coatings

MDPI

Article

Research on Laser Cladding Inconel 625 Coating Process for TRT Blades

Jian-Tao Yao, Guo-Dong Zhang *, Ze-Lin Chen, Yu-Hu Qu, Li-Shuang Wang and Hui Dong

School of Materials Science and Engineering, Xi'an Shiyou University, Xi'an 710065, China; jiantaoyao@xsyu.edu.cn (J.-T.Y.); 202112060114@stumail.xsyu.edu.cn (Z.-L.C.); 23211050709@stumail.xsyu.edu.cn (Y.-H.Q.); lswang@xsyu.edu.cn (L.-S.W.); donghui@xsyu.edu.cn (H.D.)
* Correspondence: 22211050724@stumail.xsyu.edu.cn

Abstract: In this study, Inconel 625 coatings were deposited onto the surface of 2Cr13 stainless steel via laser cladding technology to ensure their corrosion resistance and mechanical properties. The microstructure and characteristics of coatings were adjusted by varying laser power (1200, 1500, and 1800 W), scanning speed (10, 15, and 25 mm/s), and overlap rate (40%, 50%, and 70%). The results showed that the impact resistance of blades was improved by 23% to 30% compared to the substrate, whereas the self-corrosion current density was reduced by 94%–98%, which indicated the outstanding resistance of specimens to damage and corrosion. At the same time, the appropriate processing parameters enabled the surface hardness of the 2Cr13 substrate to be improved. This study provides practical technical guidance for the repair of 2Cr13 blades and a comprehensive enhancement of their corrosion resistance and mechanical properties through parameter optimization.

Keywords: laser cladding; Inconel 625; structure; corrosion resistance

Academic Editors: Rafael Comesaña and Roberto Teghil

Received: 23 December 2024
Revised: 14 January 2025
Accepted: 30 January 2025
Published: 3 February 2025

Citation: Yao, J.-T.; Zhang, G.-D.; Chen, Z.-L.; Qu, Y.-H.; Wang, L.-S.; Dong, H. Research on Laser Cladding Inconel 625 Coating Process for TRT Blades. *Coatings* **2025**, *15*, 171. https://doi.org/10.3390/coatings15020171

1. Introduction

2Cr13 steel is a low-cost martensitic stainless steel with good basic corrosion resistance and high-temperature stretchability, which finds application in tools operating under severe mechanical and corrosive conditions, such as rotor blades, fastening bolts, shafts, bushings, and hydraulic valves [1]. Moreover, 2Cr13 is often used as a TRT (blast furnace top gas recovery turbine unit) blade material [2]. However, as the blast furnace gas contains corrosive media (sulfur and chloride ions), the exposure to even small amounts of water vapor and particulate matter often leads to chemical or electrochemical corrosion and wear of the unit, affecting the safety of the whole equipment [3,4]. Therefore, it requires the development of an effective surface protection technology so as to adopt the blade to the harsh operating conditions and improve its service performance.

The corrosion resistance of a blade can be enhanced through the various technologies such as electrodeposition [5], physical vapor deposition [6] (PVD), thermal spraying [7], and laser cladding coating [8]. Among these methods, laser cladding stands out due to its ability to create a strong metallurgical bond between the coating and the substrate, resulting in enhanced corrosion resistance and mechanical properties. Unlike electrodeposition, which is limited to conductive materials and may have lower bond strength, laser cladding can be applied to a wider range of materials, including non-conductive ones, and achieves higher bond integrity. Furthermore, compared to thermal spraying, which can introduce porosity into the coating leading to potential corrosion paths, laser cladding produces denser coatings with fewer defects. PVD, while offering good adhesion, may not be as efficient in terms of material utilization and can be more expensive for certain applications.

In conclusion, while each method has its merits and may be suitable for specific scenarios, laser cladding offers a robust solution for enhancing the corrosion resistance of blades, particularly in demanding environments where high performance and reliability are crucial.

For instance, Yaseen et al. [9] employed electrodeposition to produce a Ni-SiO_2-TiO_2 composite coating with an average particle size of 30–70 nm on a steam turbine blade. The Ni-SiO_2-TiO_2 composite layer exhibited a stable structure with outstanding crystallization and surface mechanical bonding due to the good interconnection between SiO_2-TiO_2 particles and the nickel matrix. Wen et al. [2] obtained composite coatings by depositing a Ni60 binder layer and NiCrMoY top layer onto a TRT 2Cr13 steel blade via the SAPS technique. The subsequent vacuum remelting of the coatings effectively improved their bonding strength and corrosion resistance. Zhang et al. [10] used laser melting cladding to prepare a NiCrAlTi alloy coating on a 304 stainless steel substrate. The test results revealed that the corrosion resistance of the coating was 1.8 and 1.2 times higher than those of 304 stainless steel and Inconel 625 coating in an acidic environment, respectively. The NiCrAlTi alloy coating with a three-layer oxide film structure of Al_2O_3, Cr_2O_3, and TiO_2 showed a higher value for long-term or high-temperature chloride corrosion than an Inconel 625 alloy coating with a single-layer Cr_2O_3 structure.

Meanwhile, numerous attempts have also been made to improve the service performance of the coating by adjusting the processing parameters and changing reinforcing elements. Dai et al. [11] produced an Fe-13Cr-7Al coating via laser cladding onto a 12Cr1MoV substrate. According to their study, the laser power of 1875–2250 W, scanning speed of 33–44 mm/s, and powder feeding of 12–18 g/min enabled the formation of defects such as porosity and cracks to be avoided, as well as an improvement in the high-temperature corrosion resistance of the coating by a factor of 1 compared with that of the substrate. Wang et al. [12] prepared Inconel 625 coatings on the surface of 15CrMo alloy steel via laser cladding. Experimental results indicated that an optimal linear energy range of 10.8–14.4 W-min/mm and a powder feeding density range of 0.125–0.16 g/mm yielded high-quality coatings with well-formed structures, refined grains, and enhanced microhardness.

The corrosion resistance of Inconel 625 is mainly influenced by the solid solution strengthening of the matrix phase (γ′ phase), elements such as Cr and Mo, as well as by the addition of Nb and the formation of NbC precipitates. Cr significantly improves the resistance of the alloy to pitting and crevice corrosion through the formation of passivation films, whereas Mo enhances the alloy's corrosion resistance in chloride environments. Canming et al. [13] investigated the effect of Nb addition on the structure and corrosion resistance of laser-melted Inconel 625 coatings. The findings showed that the coating structure underwent transformation from coarse to isometric crystals, whereas the microhardness gradually increased with the increase in Nb content. The best corrosion resistance was achieved in 3% Nb coatings, and one of the reasons for this was the formation of NbC crystals, whereby Cr was released from the carbonized state and dissolved in the Ni phase, improving the passivation ability of the coating in the electrolyte. By optimizing the amount of Nb added and controlling the distribution of the precipitates, the corrosion resistance of the Inconel 625 coating is further enhanced, resulting in even better performance in corrosive environments.

Wang et al. [14] investigated the corrosion behavior of laser-melted Inconel 625 coatings in a high-temperature acidic environment. They inferred that the synergistic effect of Cl, S, F, and Br in the corrosive media exacerbated damage to the oxide film structure, leading to cracking and detachment, which significantly shortened the coating's lifespan. Taheri et al. [15] produced NbCrFeNiCoMoX (X = 0, 0.25, 0.5, 0.75, 1) high-entropy alloy (HEA) coatings on a GDT-111 high-temperature alloy via laser melting. Special attention

was paid to the effect of the Mo molar ratio on the corrosion resistance of coatings. The most optimal corrosion resistance was achieved at the Mo content of 0.75, whereby the amount of FCC phase decreased and those of eutectic and Laves phases increased. Meanwhile, with a further increase in Mo content, there was a drop in corrosion resistance due to the fineness of the eutectic phase. Xu et al. [16] used laser cladding technology to prepare an Fe-Mn-Si-Cr-Ni-χ (VC) shape-memory alloy (SMA) composite coatings on the surface of 42CrMo steel. Their results showed that the coatings were mainly composed of the γ austenite (FCC) phase and ε martensite (hcp) phase. The addition of VC to the shape-memory alloy promoted the γ → ε martensite phase transition, and the maximum polarization resistance of the coating was 4.39 times that of the matrix at the VC amount of 1.5%, which greatly improved the corrosion resistance. Zhang et al. [17] prepared Fe0.25Co0.25Ni0.25Cr0.125Mo0.125 86B14 HEA coatings via laser melting and explored the effects of annealing temperature on the composition, structure, corrosion resistance, and wear resistance of different parts of the coating (top, middle, and bottom). The results showed that the coating annealed at 800 °C exhibited the greatest hardness, the lowest friction coefficient and wear volume loss, and the best corrosion resistance in each examined section.

Laser cladding is the advanced surface modification technology that consists of the laser melting of a powder under a certain pressure of gas, whereby the melted powder is deposited onto the surface of a workpiece. In the presence of some of the laser energy, a partially melted parent material forms a cladding layer that is linked with the substrate through a high bonding force [18]. Inconel nickel-based alloys as leaders in the field of high-temperature alloys play an irreplaceable role in many fields, such as the aerospace and petrochemical industries, nuclear energy, and medical treatment, which is due to their excellent corrosion resistance, high-temperature strength, and oxidation resistance. Among them, attention is paid to Inconel 625 alloy whose outstanding anti-oxidation and anti-corrosive properties find application in high-stress and high-temperature environments, such as engine components, and turbine discs and seals [1,19].

However, due to the particular molding principle of laser cladding, the molten pool formation and the cooling rate during the cladding are too fast, which can easily promote defects (e.g., pores and cracks) in the cladding layer, affecting its service performance. Therefore, improving the performance of the cladding layer by adjusting the microstructure of the laser cladding layer and reducing its internal defects has recently become a hot research topic. In this study, Inconel 625 coatings were prepared on 2Cr13 substrates via laser melting, and the effects of different melting parameter powers (power: 1200, 1500, and 1800 W; scanning speed: 10, 15, and 25 mm/s; and overlap rate: 40%, 50%, and 70%) on the structure and properties of the coatings were investigated.

2. Materials and Methods

2.1. Materials and Coating Preparation

A heat-treated 2Cr13 steel (Tianyuan Shaanxi Limited by Share, Ltd., Xi'an, China) (110 mm × 100 mm × 10 mm) was used as the substrate (details regarding its chemical composition and mechanical properties are given in Tables 1 and 2). 2Cr13 steel is heat treated according to the standard GB/T 1220-2007 'Stainless Steel Bar' [20]; the specific heat-treatment conditions are quenching at 1000 °C, holding for 40 min with oil cooling, and then tempering at 650 °C, holding for 60 min with air cooling. Inconel 625 powder (Beijing Ryubon New Material Technology Co., Ltd., Beijing, China) was employed to prepare the laser fusion coatings (the range of particle sizes is shown in Figure 1, the powder morphology is shown in Figure 2, and the composition is summarized in Table 3).

Table 1. Chemical composition of 2Cr13 stainless steel (wt.%).

Element	C	Si	Mn	S	P	Cr	Cu	Ni	Fe
wt.%	0.2	0.38	0.52	0.001	0.025	13.0	0.08	0.44	Balanced

Table 2. Mechanical properties of 2Cr13 stainless steel after heat treatment.

Materials	Yield Strength/MPa	Tensile Strength/MPa	Elongation/%	Section Shrinkage/%	Impact Energy AK_V (J/20 °C)
2Cr13	598.0	754.0	21.4	63.9	148.2

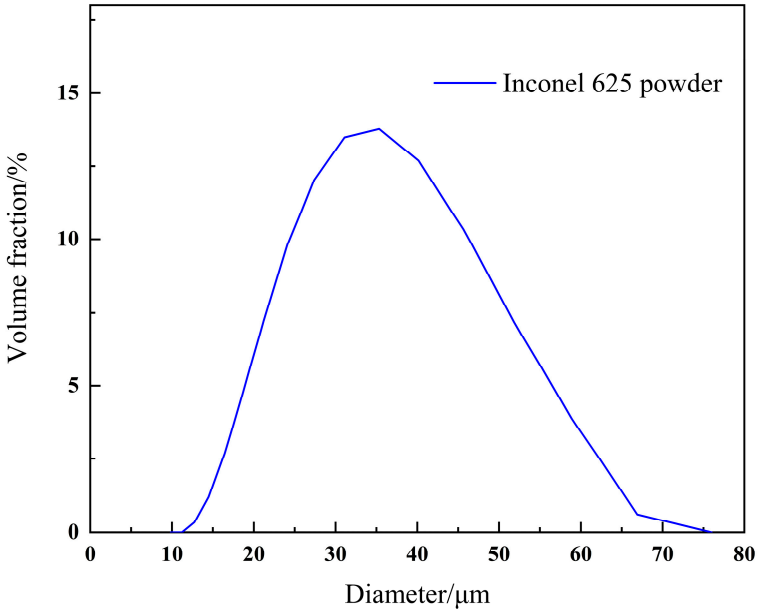

Figure 1. Inconel 625 powder particle size.

Before laser cladding, the powder was dried in a muffle furnace at 100 °C for 2 h. The substrate was roughened, degreased, and descaled. The coatings were prepared using laser melting equipment (JHM-1GX-3000P) (Zhejiang HIGHLASER Technology Co., Ltd., Rui'an, China). The corresponding laser cladding parameters are listed in Table 4.

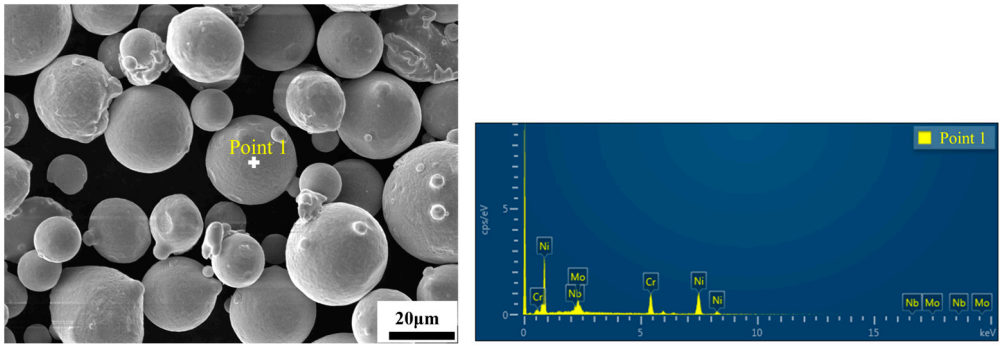

Figure 2. Inconel 625 powder morphology and EDS spectrum.

Table 3. Inconel 625 powder composition.

Elemental	Ni	Cr	Nb	Mo	Fe	Ti	Si	Al	C
wt.%	Bal.	22.82	4.02	10.57	≤5	≤0.4	≤0.5	≤0.4	≤0.1

Table 4. Laser coating parameters.

Samples	Laser Power (W)	Scanning Speed (mm/s)	Overlap Rate (%)	Spot Diameter (mm)
1#	1200	20	70	2 mm
2#	1500	20	70	
3#	1800	20	70	
4#	1500	10	70	
5#	1500	15	70	
6#	1500	25	70	
7#	1500	20	40	
8#	1500	20	50	
9#	1500	20	70	

2.2. Electrochemical Properties

The corrosion properties of the polished fusion-coated coatings were tested using a typical three-electrode system with a CS310H electrochemical workstation (Wuhan Corrtest Instruments Corp., Wuhan, China). In this case, the coating, platinum electrode, and saturated calomel electrode (SCE) served as working, auxiliary, and reference electrodes, respectively.

Prior to the electrochemical test, the surface of the coating was sanded and polished. The polished samples were then immersed in alcohol, ultrasonically cleaned for 10 min, and blow-dried under compressed air. The samples with an area of 1 cm^2 were then exposed to electrochemical corrosion testing using Potentiodynamic Polarization (PDP) in 3.5 wt.% NaCl solution for 1 h. The test temperature of the solution was always maintained at 25 ± 2 °C. Once the open-circuit potential was stabilized, the coating impedance and polarization current were measured via the dynamic potential polarization tests at a voltage scanning rate of 0.5 mV/s. The EIS data were fitted to obtain the corrosion current density (Jcorr).

2.3. Microhardness

A HXD-1000TMC micro Vickers hardness tester (Shanghai Optical Instruments Co., Ltd. No. 6., Shanghai, China) was employed to assess the Vickers hardness of the coating. Before the test, the surface was gradually polished to 1500 mesh using sandpaper to ensure that the specimen could be placed horizontally. After this, the tests were conducted from the top of the fusion cladding layer to the substrate by applying a load of 300 g for 15 s, while the distance between the two neighboring test points was kept the same at 90 μm.

2.4. Impact Resistance Test

The impact resistance of specimens (55 mm × 10 mm × 10 mm) was measured at room temperature in accordance with GB/T229-2020 standard [21], using an ENY-T100 digital pendulum impact tester (Ruiwen Instruments Co., Ltd., Guangzhou, China) with a 45° V-notch, as shown in Figure 3.

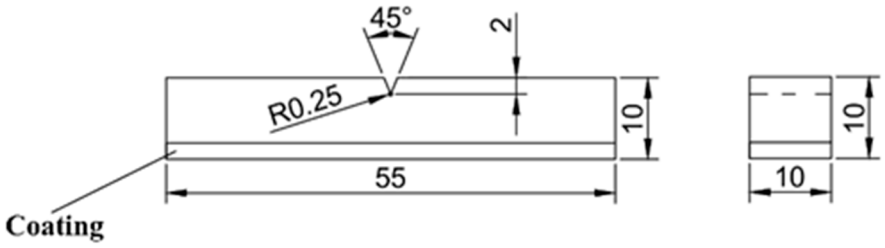

Figure 3. Schematic diagram of a standard size impact specimen.

3. Results and Discussion

3.1. XRD Analysis

Figure 4 depicts the XRD spectra of the 2Cr13 substrate, Inconel 625 powder, and cladding layers. By comparing the XRD data with the ICDD database, it was found that the 2Cr13 matrix was mainly composed of the α-Fe phase, and the cladding layers were made of γ-Ni phases. The detection of the γ-Ni phase is consistent with the results of Feng et al. [22].

According to the ICDD database, the peak positions for the FCC Ni phase are 2θ of 44.5°, 51.9°, 76.4°, 92.9°, and 98.5°. This suggests that the primary phase in the cladding is γ-Ni, and the minor differences in peak positions are due to the alloying elements in the solid solution of Inconel 625 cladding. This affected the inter-planar spacing of the γ-Ni present in the coating. The γ′, γ″, and Laves was not detected, possibly because its volume fraction was below the XRD detection limit (approximately 1%–2%). On the other hand, the peak shift is also possible due to residual stress present in the γ phase. In addition, phases such as Cr_2O_3 and $NiCr_2O_4$ were detected in 1#, 2#, 6#, and 7#, which may be the oxides of the surface Stargall during the high-temperature process.

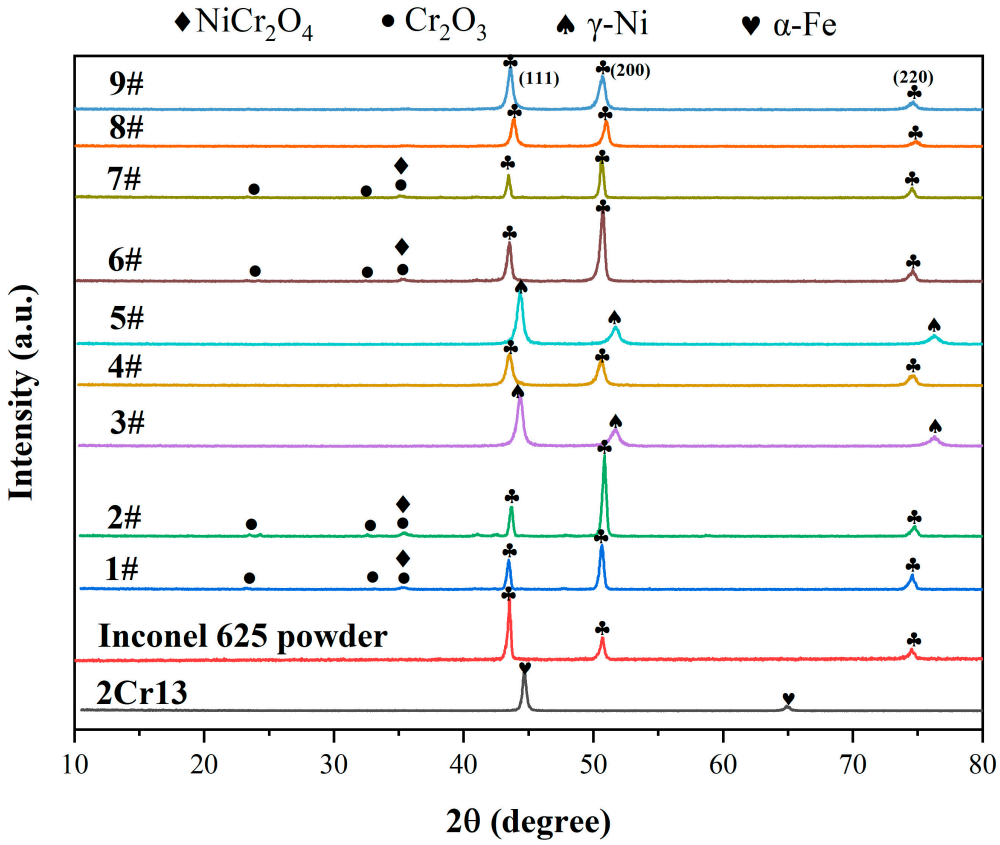

Figure 4. XRD spectra of Inconel 625 coatings, Inconel 625 powder, and 2Cr13 substrate.

3.2. Morphology of the Cladding Layer

Figure 5 depicts the cross-sectional morphology of the interfaces of laser-melted Inconel 625 coatings at different processing parameters. Except for the 4# sample (scanning speed of 10 mm/s), there were no defects such as pores and cracks inside the coatings, and there was a continuous metallurgical bonding interface between the cladding layer and the substrate. The cross-section of the 4# cladding layer reveals a large number of unfused pores at the interface.

Slow scanning speeds can result in the exposure of localized areas to high temperatures for extended periods of time, which promotes excessive evaporation of the Inconel 625 material. This can form bubbles in the melt pool, which may not have time to overflow during the rapid solidification, causing the formation of pores at the coating–substrate interface [23].

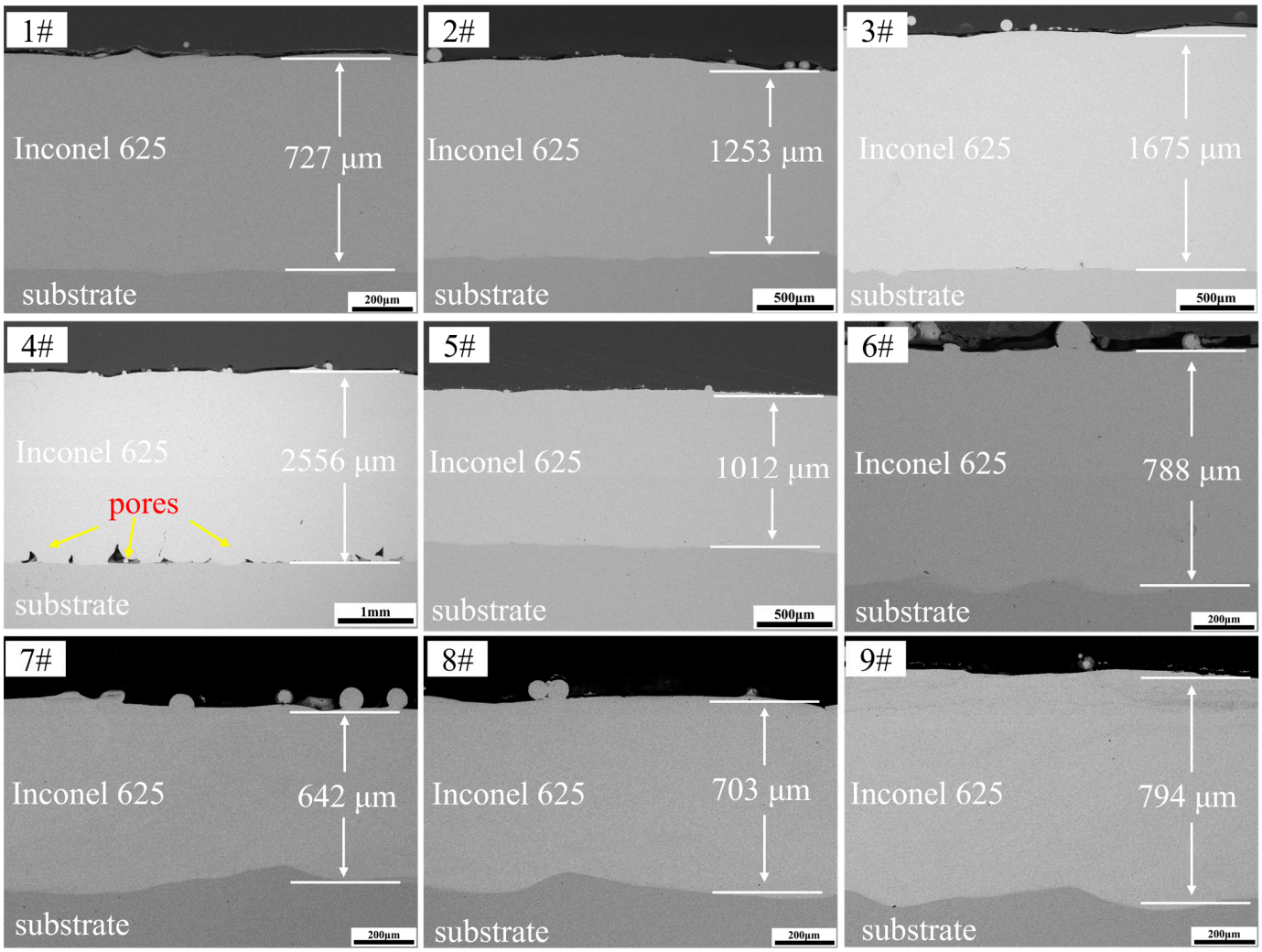

Figure 5. Cross-sectional morphology of laser-cladded Inconel 625 coatings.

Unfused pores at the interface are voids between the substrate and the coating or joining layer that have not reached full fusion [24]. The presence of these voids can have a significant negative impact on the overall performance and safety of materials and components, causing the following hazards to the interface.

(1) Deterioration of mechanical properties

Interfacial unfused pores weaken the bond strength between the substrate and the coating. Under stress, the interface region is more likely to fail, leading to a reduction in the overall structural strength [25].

Besides that, unfused pores will act as sources of crack initiation and propagation, easily triggering brittle fractures when the structure is subjected to impact loads.

(2) High corrosion risks

The pores tend to accumulate moisture and corrosive media from the environment, causing chemical or electrochemical corrosion, which leads to interfacial corrosion and affects the corrosion resistance of the overall structure [12].

If the pores at the interface are connected to the side surface of the substrate, the external corrosive medium can expand to the interior through the pores, thus extending the internal corrosion.

Therefore, effectively reducing or eliminating the pores between the interfaces of laser cladding coatings can improve the overall performance and reliability of the coating.

Figures 6–8 display the structure and morphology of all Inconel 625 coatings after aqua regia corrosion in an HCl:HNO_3 (3:1) solution for 90 s.

Figure 6 depicts the microstructures of 1#–3# coatings, revealing the effect of different laser powers on the structure and morphology of cladding layers of Inconel 625 alloy.

Once the laser power increased from 1200 to 1800 W, the microstructure of the Inconel 625 alloy cladding layer gradually transitioned from fine grains to large-sized columnar crystals. In particular, at 1200 W, the rapid cooling resulted in the formation of fine grains at the top, elongated grains in the middle, and columnar crystals at the bottom of the layer. At 1500 W, the grains increased at the top, and columnar crystals were more pronounced and denser in the middle and bottom of the layer. At 1800 W, the grains continued to increase, and the columnar crystals in the middle and bottom tended to be continuous. This indicates that the heat input from the higher power significantly affects the crystalline behavior and tissue morphology.

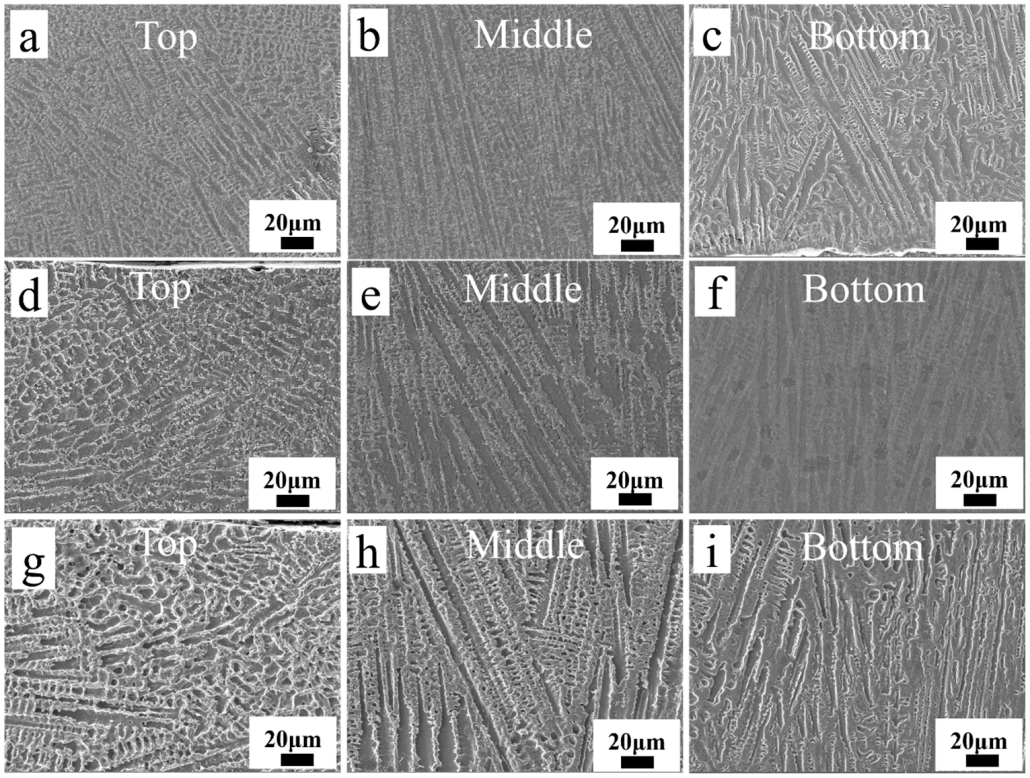

Figure 6. Microstructure of 1# (**a**–**c**), 2# (**d**–**f**), and 3# (**g**–**i**) coatings.

Figure 7 displays the impact of different scanning speeds on the microstructures of 4#–6# coatings.

With increasing cladding speed, the near-surface temperature gradient $|G_L|$ of the cladding layer increases, the solidification rate R increases, and the cooling speed increases [26]. The microstructure of the samples gradually changed from coarse columnar crystals to fine isometric crystals. Low scanning speeds (e.g., 4# sample) caused heat accumulation and the formation of coarse columnar crystals. Medium scanning speeds (e.g., 5# samples) produced uniform fine columnar crystals, while high scanning speeds (e.g., 6# samples) were conducive to grain refinement due to rapid cooling, leading to the emergence of small uniform isometric crystals.

Therefore, the findings showed that different scanning speeds significantly affected the microstructure of cladding layers of Inconel 625 alloy. The slower scanning speed (10 mm/s) resulted in larger columnar crystals in the cladding due to the higher heat input, whereas the faster scanning speed (25 mm/s) induced grain refinement owing to the rapid cooling effect from the reduced heat input.

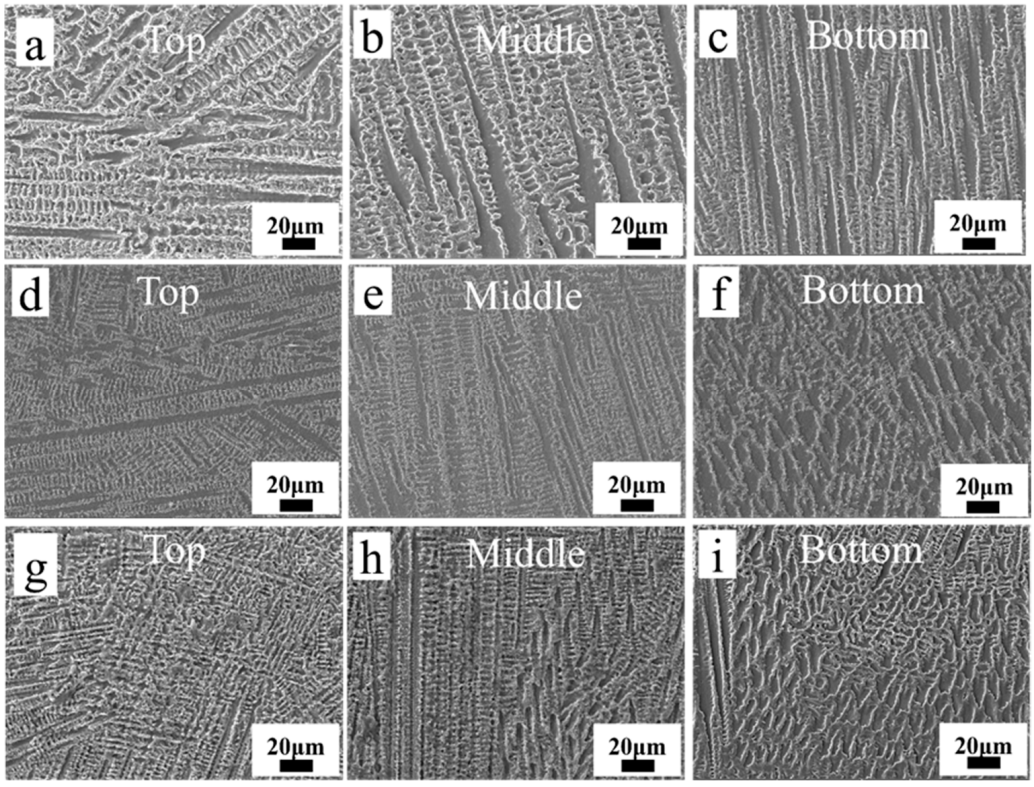

Figure 7. Microstructure of 4# (**a**–**c**), 5# (**d**–**f**), and 6# (**g**–**i**) coatings.

Figure 8 depicts the microstructures of 7#–9# coatings at various overlap rates.

The grain structure of the samples became progressively coarser as the overlap ratio increased. Low overlap rates (e.g., sample #7) resulted in smaller heat-affected regions and the formation of finer equiaxed or columnar crystals. Medium overlap rates (e.g., sample 8#) promoted uniform grain growth. Finally, high overlap rates (e.g., 9# sample) promoted grain coarsening because of heat accumulation, forming a more pronounced columnar crystal structure.

Thus, the different overlap rates had a noticeable effect on the microstructure of Inconel 625 laser cladding layers. A low overlap rate (40%) led to the formation of fine and homogeneous particles due to less heat accumulation, whereas a high overlap rate (70%) contributed to the emergence of larger columnar crystals, which exhibited a strong heat accumulation effect. This implies that the microstructure of the coating can also be tuned by properly adjusting the overlap ratio.

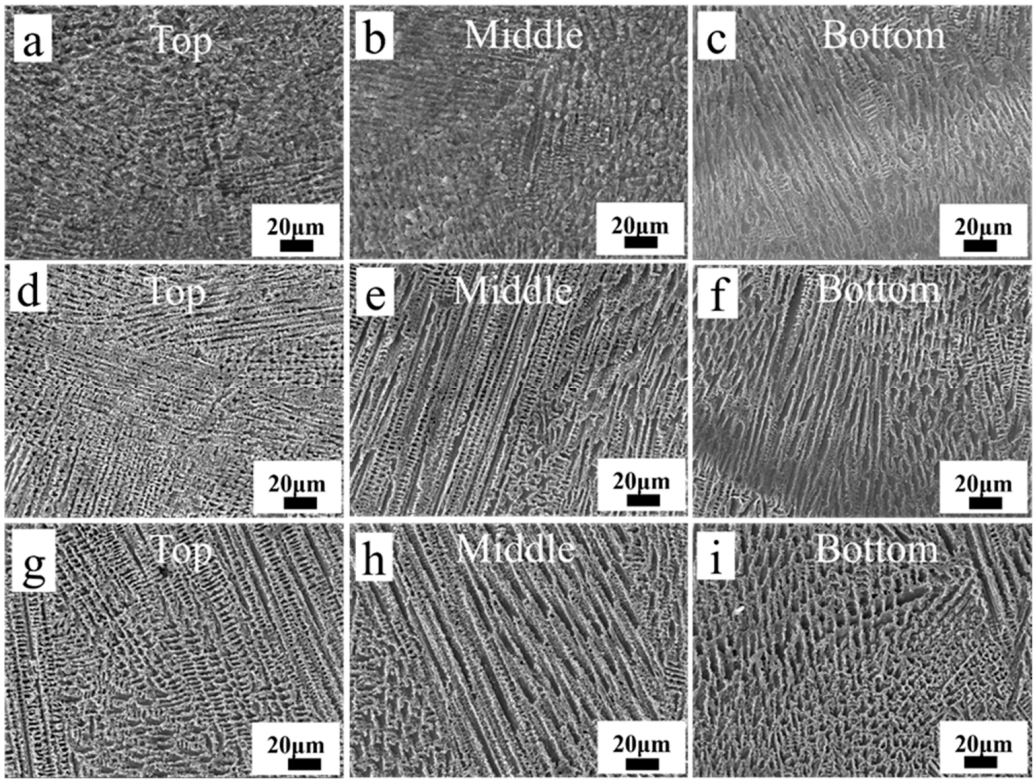

Figure 8. Microstructure of 7# (**a**–**c**), 8# (**d**–**f**), and 9# (**g**–**i**) coatings.

EDS elemental analyses are shown in Figure 9. The grain size of the cladding layer changed with the cooling rate, and the grains gradually increased from the surface of the cladding layer toward the substrate. The top possessed a uniformly dense and homogeneous structure composed of fine columnar and equiaxial crystals due to the faster cooling rate. In the middle region, the cooling rate slowed down, and the coarse columnar crystals or dendrites were observed in some parts. Finally, there was columnar/dendritic crystal growth in the bottom region, owing to the greater heat input close to the matrix. Under rapid solidification conditions, elemental diffusion is limited due to the short time, which tends to cause certain elements with a more uniform distribution in the melt pool to form local enrichment at grain boundaries during solidification, especially those elements with high solidification partition coefficients, e.g., Mo and Nb, which tend to concentrate more in the grain boundary region of the final solidification, leading to the phenomenon of segregation. In addition, the large atomic radii of Mo and Nb, which differ significantly from the atomic size of the matrix elements (e.g., Ni), result in relatively low diffusion rates in the melt. During rapid cooling, these low diffusion rate elements cannot diffuse rapidly into the crystal but are more likely to accumulate at grain boundaries and form segregation zones. The enrichment of these elements at the grain boundaries is conducive to improving the strength of the grain boundaries, thus improving the high-temperature mechanical properties of the composite coatings.

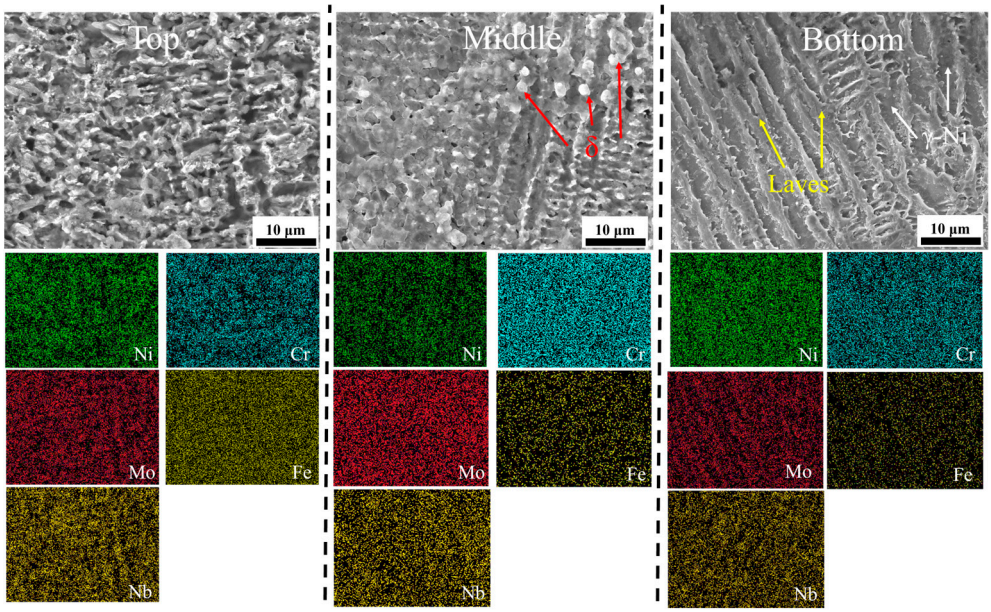

Figure 9. EDS mappings of element of coating.

3.3. Corrosion Resistance

Generally, the commonly used free corrosion potential and free corrosion current density are used to evaluate the corrosion likelihood of the material. The corrosion current caused by the dissolution of the material reflects the speed of corrosion: the smaller the corrosion current density is, the slower the corrosion rate of the material and the better its corrosion resistance.

To further obtain the polarization curves, the polished specimens were placed in a 3.5 wt.% NaCl solution under an applied current. Figure 8 shows the EIS results for the 2Cr13 substrate and coatings at different laser melting parameters. Figure 8a shows the Nyquist plots of the laser-fused cladding and 2Cr13 steel, Figure 10b zooms in on the Nyquist plot of 2Cr13 steel, and Figure 10c shows the polarization curves, and it can be noticed that the 2Cr13 has a low impedance value compared to the fused cladding. A lower impedance value means that the material surface is less protected during the electrochemical reaction and is more prone to corrosion reactions.

The experimental polarization curves were fitted according to the Tafel linear extrapolation method to calculate the corrosion potentials and corrosion current densities of the coatings, and the data are displayed in Table 5.

Corrosion potential is the stable electrode potential of a material in a particular environment. The more positive the corrosion potential is, the better the corrosion resistance of the material. As can be seen from Table 5, the 2Cr13 substrate possessed the lowest corrosion potential (−0.735 V), indicating that coatings were conducive to the increase in the corrosion resistance.

The corrosion current density reflects the corrosion rate of the material during the corrosion process. The smaller the value is, the better the corrosion resistance of the material and, therefore, the lower its corrosion rate. The corrosion current density of the 2Cr13 substrate was 6.32×10^{-6} A·cm^{-2}, which was considerably higher than those of the coated samples (3.51×10^{-7}–1.24×10^{-7} A·cm^{-2}), meaning the corrosion current density values in the coated samples were generally lower, and the lower the corrosion current density, the better the corrosion resistance in the corrosive environment.

The test results showed that the self-corrosion potential of the 2Cr13 stainless steel was −0.735 V. In turn, the self-corrosion potential of Inconel 625 coatings prepared via laser cladding was positively shifted from 0.403 to 0.501 V. Given also a dramatic decrease

in the corrosion current density of the coatings (by 94%–98%), laser cladding enabled the corrosion resistance of the base material to be greatly improved.

Compared with the polarization curve studied by Guo et al. [27], it was found that all the laser cladding layers prepared in this study exhibited a more positive Ecorr and smaller Icorr compared to the single-layer Inconel 625 cladding layer deposited using pulsed tig welding. This suggests that the coatings prepared by laser cladding have better corrosion resistance than the single-layer Inconel 625 cladding layer deposited by pulsed tig welding.

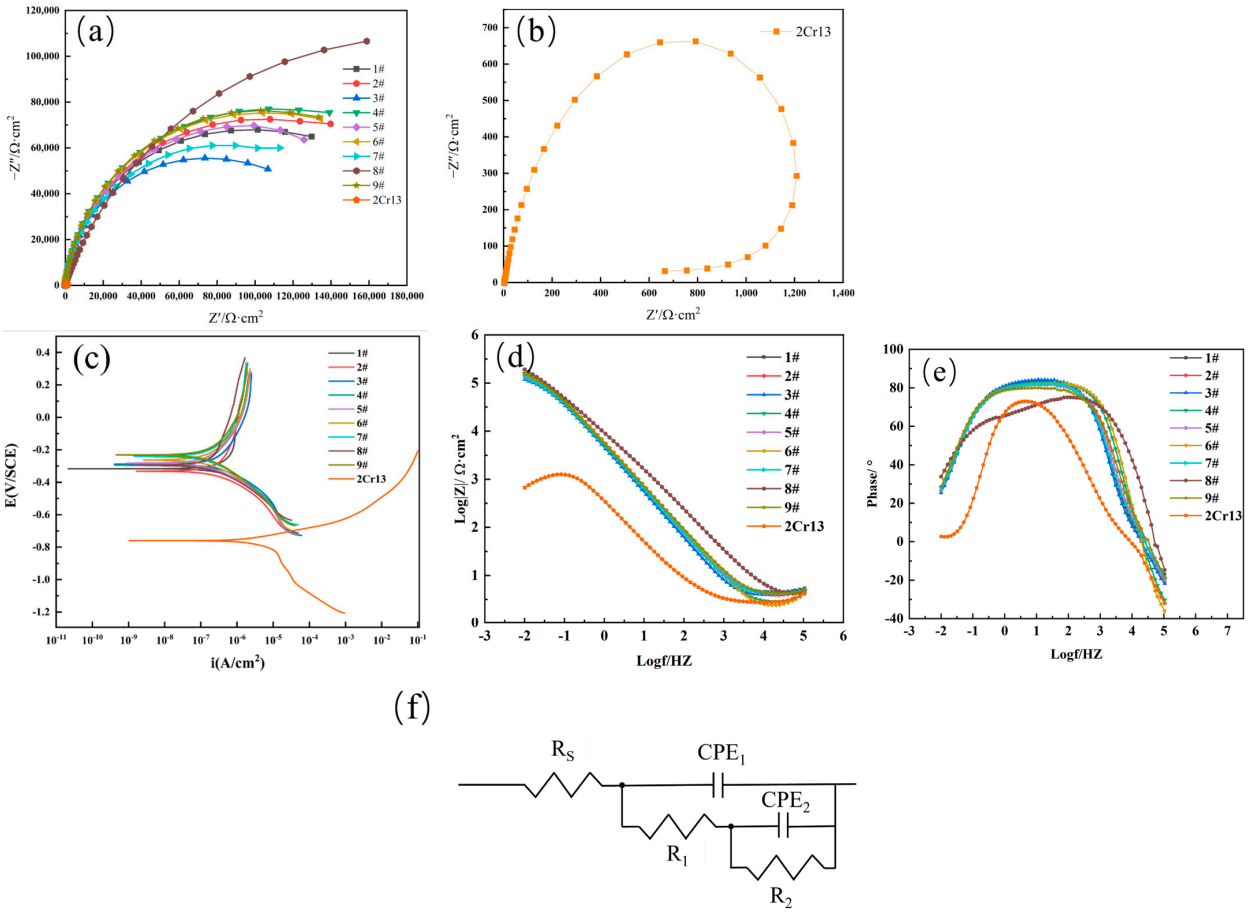

Figure 10. EIS data of 2Cr13 substrate and coatings at different cladding parameters: (**a**) Nyquist plots of cladded coatings; (**b**) Nyquist plots of 2Cr13; (**c**) polarization curves of cladded coatings and 2Cr13; (**d**) Bode phase plots; (**e**) Bode impedance plots, and (**f**) equivalent circuit.

Table 5. Electrochemical parameters used in fitting of polarization curves acquired from Inconel 625 alloy in 3.5% NaCl solution.

Sample	E_{corr}/V	I_{corr}/A·cm^{-2}
2Cr13	−0.735	6.32×10^{-6}
standard Inconel 625	−0.145	0.47×10^{-7}
1#	−0.316	3.51×10^{-7}
2#	−0.330	2.29×10^{-7}
3#	−0.279	2.22×10^{-7}
4#	−0.282	1.43×10^{-7}
5#	−0.276	1.24×10^{-7}
6#	−0.263	1.30×10^{-7}
7#	−0.242	1.29×10^{-7}
8#	−0.295	1.56×10^{-7}
9#	−0.232	1.31×10^{-7}

According to the equivalent circuit component data in Table 6, the deviation χ^2 values of the fitting results for most samples are in the order of 10^{-4}, indicating that the equivalent circuits are more reasonable. The Rs values are the same, indicating that the electrode reaction process has less influence on Rs and that its value is mainly dependent on the conductivity of the electrolyte. Cf and Rf denote the capacitance and resistance of the coating or corrosion product layer, respectively, and Cdl and resistance Rct refer to the bilayer. Cdl and resistance Rct refer to the double electric layer's capacitance and charge transfer resistance, respectively; considering the dispersion effect, Q is used instead of C. The Rf value can indicate the corrosion protection effect of the coating or corrosion product layer, and a more considerable Rf value indicates that the defect density of the Inconel 625 coating is lower. Rct reflects the kinetics of the corrosion reaction, and a higher value of Rct indicates that the passivation film has fewer activation sites, which makes the electrochemical reaction rate or the rate of the reaction occurring at the interface of the Inconel 625 coating/electrolyte more efficient and effective. The rate of electrochemical reaction occurring at the interface or the dissolution rate of the coating is reduced. The smaller Cf and Cdl values indicate that the Inconel 625 coating has a smaller localized corrosion area and a thicker layer of corrosion products. Therefore, Inconel 625 showed stronger corrosion resistance in a 3.5% NaCl solution, which can significantly improve the corrosion resistance of 2Cr13 steel, consistent with the results of kinetic potential polarization tests.

Table 6. Fitting results of equivalent components.

Sample	R_s $\Omega \cdot cm^2$	CPE_f		R_f $\Omega \cdot cm^2$	CPE_{dl}		R_{ct} $\Omega \cdot cm^2$	R_p (R_{ct}+ R_f) $\Omega \cdot cm^2$	χ^2 10^{-4}
		$Y_f/10^{-6} \cdot \Omega$ $1 \cdot cm^{-2} \cdot s^n$	n_f		$Y_{dl}/10^{-6} \cdot \Omega$ $1 \cdot cm^{-2} \cdot s^n$	n_{dl}			
2Cr13	3.16	512.7	0.8695	1277	40,950	0.9967	1.5	1278.5	44.7
1#	4.72	18.49	1	125.3	16.61	0.775	1,687,000	1,687,125.3	6.8
2#	4.24	14.27	1	88.41	18.87	0.7929	1,833,000	1,833,088.4	10.2
3#	4.21	36.34	0.9508	260.0	9.70	0.5067	1,262,000	1,262,260.0	12.1
4#	3.31	16.63	1	236.5	17.05	0.7748	1,923,000	1,923,236.5	4.5
5#	4.40	16.26	1	99.28	19.77	0.7877	1,731,000	1,731,099.3	8.3
6#	3.10	16.49	1	262.5	17.91	0.7723	1,904,000	1,904,262.5	15.4
7#	4.51	17.61	1	84.09	21.09	0.7756	1,563,000	1,563,084.1	6.8
8#	4.52	35.69	1	32.61	23.33	0.7036	3,307,000	3,307,032.6	5.4
9#	4.48	12.87	1	73.53	22.42	0.8042	1,933,000	1,933,073.5	6.5

3.4. Micro Vickers Hardness

Hardness is a key indicator for evaluating a material's resistance to wear and deformation [28]. The hardness data at different laser cladding parameters are shown in Figure 11. According to the results, the hardness of the fused cladding layer varies very little at different cladding parameters. The average hardness of the coatings is about 250 HV. This indicated that coatings formed via laser cladding had a stable hardness. This result is comparable to the hardness of Inconel 625 coatings prepared using laser cladding by Feng et al. [22].

The hardness of the heat-affected zone generally increases compared to the substrate due to the rapid cooling during the cladding process, which produces a needle-like quenched hard and brittle phase martensite in the vicinity of the melting zone of the substrate, and a large number of supersaturated alloying elements precipitate out into the martensite in the form of metal carbides and so on, which will make the microhardness of the heat-affected zone increase.

The overlap rate has a large influence on the hardness change in the heat-affected zone, and the increase in the overlap rate from 40% to 70% for samples 7#–9# shows an overall

decreasing trend in the hardness of the heat-affected zone, mainly due to the fact that the increase in the overlap rate leads to higher heat input and a lower thermal cooling rate, and the grains may grow larger, which usually results in a decrease in the hardness [29].

The hardness values of all samples decreased to around 150 HV, reflecting the relatively low hardness of the substrate itself, compared to the Inconel 625 coating.

Laser cladding can compensate for the defects of the 2Cr13 substrate by improving the hardness of the surface. In this respect, elucidating the effect of different parameters on the hardness enables optimization of the coating process so as to enhance surface hardness and wear resistance.

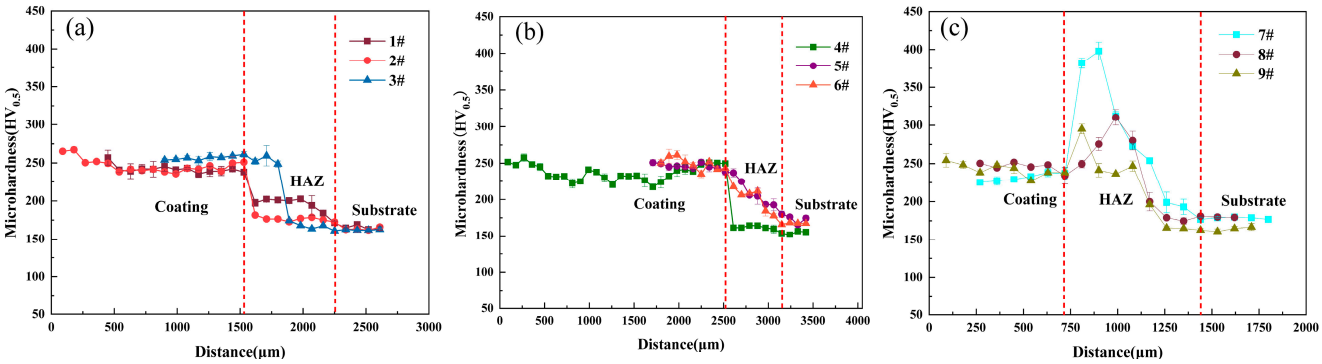

Figure 11. Hardness of (**a**) 1#–3#, (**b**) 4#–6#, and (**c**) 7#–9# samples.

The structure and hardness of the coated layer can be adjusted through different combinations of laser power, scanning speed, and overlap rate. This flexibility allows the process to be adapted to the specific usage environment of the blade and to ensure its maximum performance.

Therefore, the proper optimization of the laser cladding process is beneficial for the improvement in hardness and overall performance of the 2Cr13 blade surface, providing a more durable solution for practical applications.

Spectroscopic scanning of the sample cross-section revealed a gradient distribution of Cr, Fe, Ni, Nb, and Mo in the transition region between the coating and the substrate. This indicates the transition of elements within the coating to the substrate. Cr elements are present in higher levels in the coating and then gradually decrease in the HAZ region until they reach a constant value in the substrate. The elements Fe and Ni are present at low levels in the coating region but show a steep increase in the HAZ region and then remain relatively constant in the substrate. The distribution curves of the elements Nb and Mo do not change significantly between the coating and the substrate but are present in some amount throughout the region. The elemental distribution curves in the HAZ region show an obvious gradient transition, indicating that during the cladding process, obvious diffusion and phase transformation occurred due to the different compositions of the coating and the substrate.

During the cladding process, the temperature of the material in the HAZ region increased rapidly and then cooled rapidly, and this rapid cooling process led to transformations in the microstructure, including the formation of hardened phases such as martensite. Meanwhile, the redistribution of elements in different regions during the cladding process is an important factor affecting the hardness. According to the results of the elemental line scans in Figure 12, specific hardening elements (e.g., Cr and C) are concentrated in the HAZ region with respect to the substrate because the atoms gain enough energy to overcome the lattice barriers and move during the heating process; after cooling, these atoms form stable phases or produce solid solution strengthening in localized regions, which increases the local hardness values.

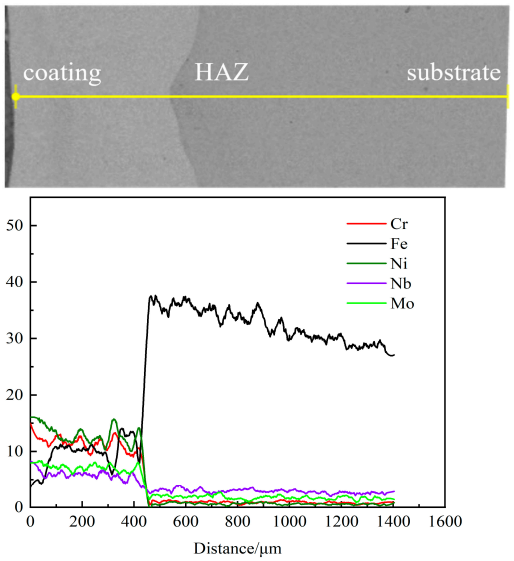

Figure 12. Distribution of elements in different regions.

Figure 13 illustrates the microstructural morphology of the HAZ and the results of the elemental surface scanning in this region, including the distribution of elements such as Fe, Nb, Mo, Ni, C, Mn, Cu, Cr, and Mo. In Figure 13a, it can be observed that the microstructure in the HAZ region consists of a long lamellar martensitic structure, which usually has high hardness and toughness. The microdetail in the HAZ region is more clear in Figure 13b, with an obvious lamellar crystalline morphology. Elements such as Cr, Mo, and C are redistributed in the material due to increased solubility at high temperatures, and the enrichment of these elements improves the hardening effect of the material. For Cr and C especially, their enrichment can increase the stability of the martensitic phase and thus improve the hardness of the HAZ region.

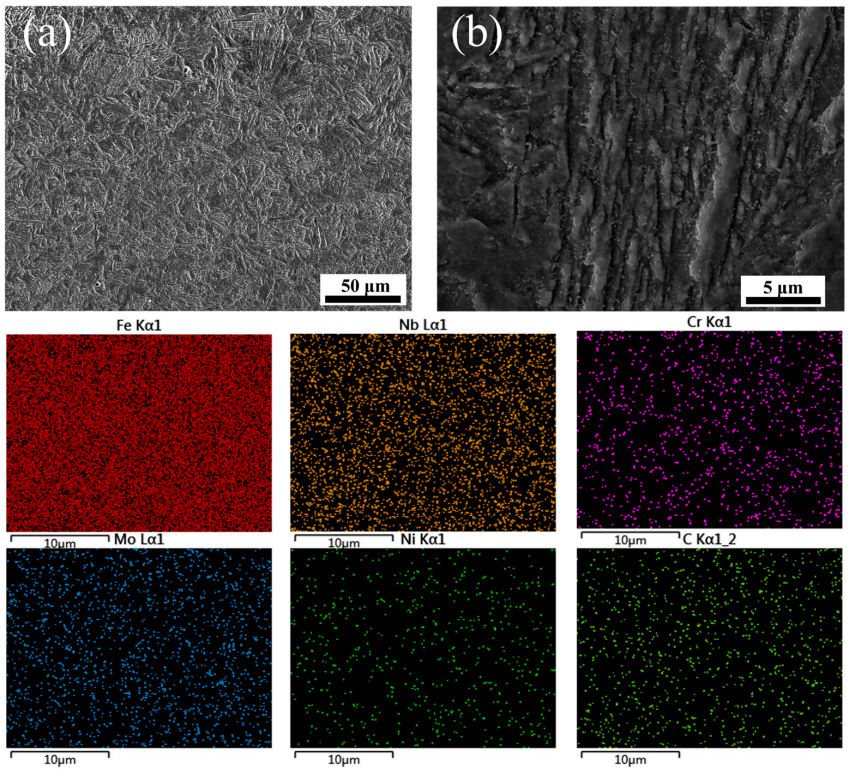

Figure 13. (**a**) HAZ microstructure (1000×); (**b**) HAZ microstructure (10,000×).

3.5. Impact Resistance

Figure 14 depicts the cross-sectional morphology of Inconel 625-coated impact specimens produced at different laser cladding parameters. All coatings exhibited a typical toughness fracture, meaning that they performed well under the impact load without obvious spalling and cracking. In a word, the improvement in toughness and bonding strength resulted in good stability under pendulum impact.

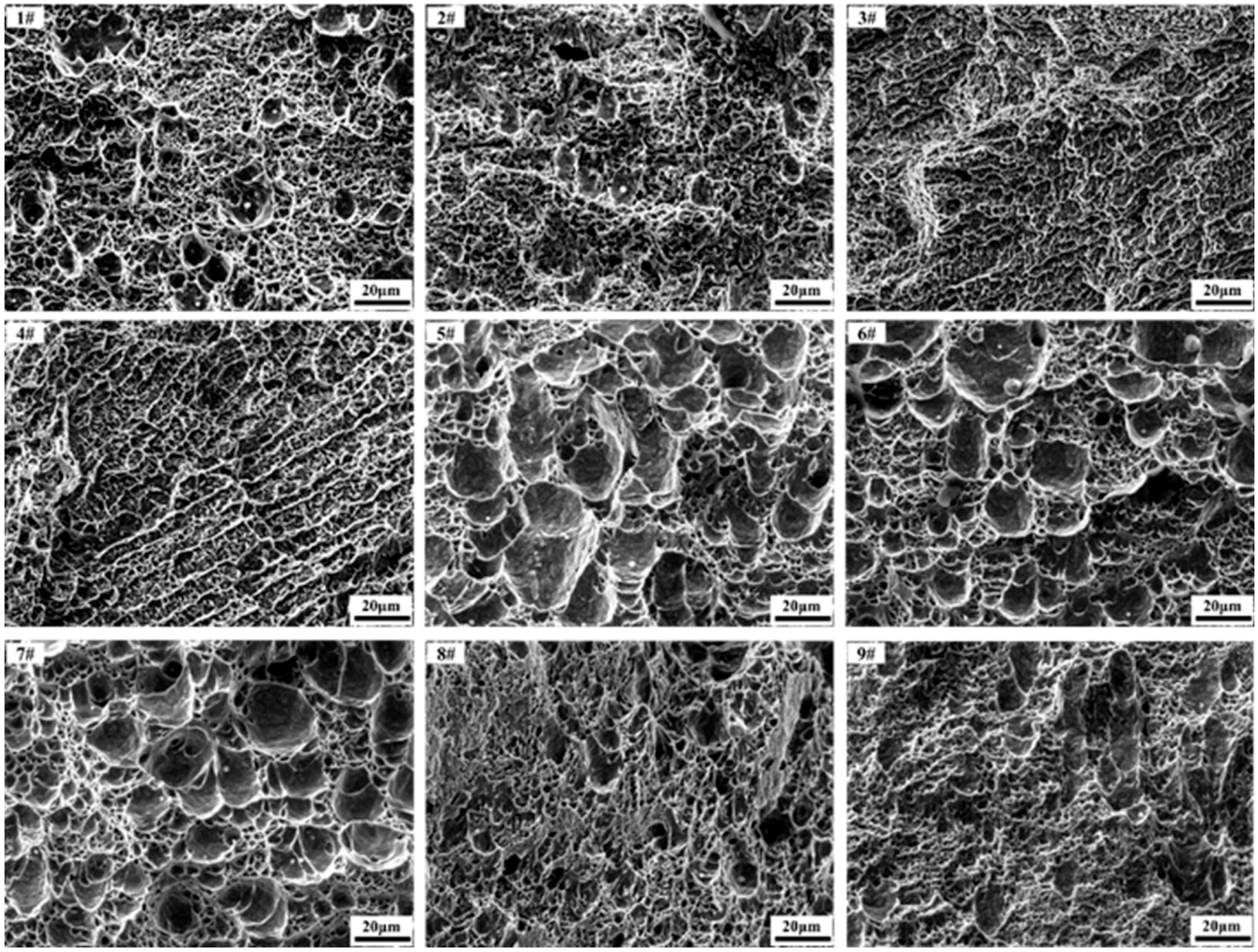

Figure 14. Cross-sectional morphology of impact specimens at different laser cladding parameters.

Figure 15 displays the impact test data. By comparing the micrographs with the impact work results, it was implied that laser fusion cladding significantly enhanced the impact toughness of the metal substrate. Since the impact performance is closely related to the microstructure, the appropriate laser cladding parameters (e.g., a combination of laser power and scanning speed) can ensure that the coating is sufficiently fused to the substrate to reduce the porosity and disintegration surfaces.

Moreover, the impact work of all the samples was much higher than that of the base material, indicating that laser cladding increased the overall impact resistance of the material, which was also reflected in the uniformity of the microstructure and the interlayer bonding. In the coatings, the highest and lowest impact work (193.2 J and 181.5 J) was achieved in samples #2 and #6, respectively, being about 30% and 23% higher than that of the substrate. Thus, laser cladding of Inconel 625 can significantly improve the impact resistance of the 2Cr13 material. Meanwhile, the analysis revealed that with the increase in power, the impact work of specimens 1#–3# varied in a non-monotonic manner, enriching

the most optimal value at 1500 W. In turn, the impact work of specimens 4#–6# slightly decreased from 186.7 to 181.5 J with the increase in scanning speed from 10 to 25 mm/s. This indicated that the scanning speed had a small effect on the impact work. Finally, the impact work of coatings 7#–9# non-monotonically changed at the overlap rate of 40%–70%, being most optimal at a 50% overlap rate.

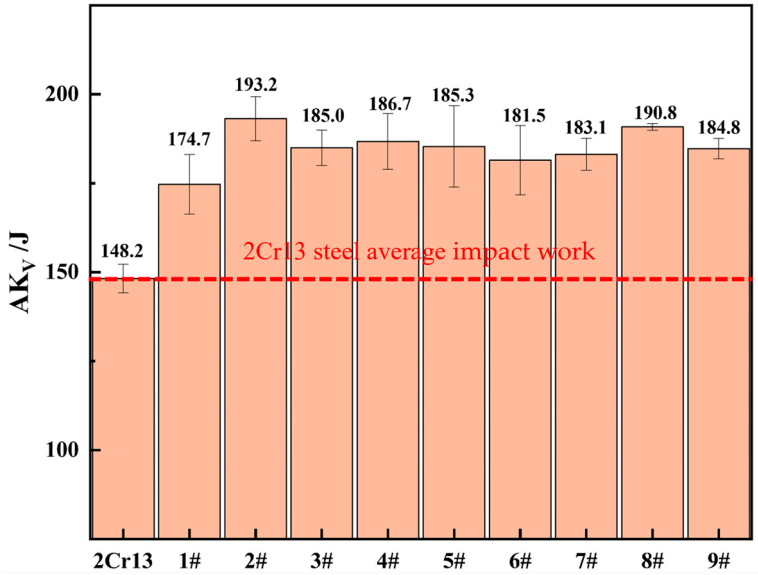

Figure 15. Impact work values of the samples for the base material and nine different laser cladding parameters (J).

4. Conclusions

The aim of this research work was to investigate the microstructure and properties of Inconel 625 coatings deposited on the surface of 2Cr13 steel with different laser cladding parameters, and based on the above experimental results, the following conclusions can be drawn:

(1) In all the coating samples, except the one exposed to a laser scanning speed of 10 mm/s, the fused cladding layer exhibited good quality and was firmly bonded to the substrate. Moreover, its structure was dense, revealing no defects such as pores, cracks, large particles of oxide inclusions, etc.

(2) The microstructure of the cladding layer changed with the cooling rate, and the grains gradually increased from the surface of the cladding layer toward the substrate. The top possessed a uniformly dense and homogeneous structure composed of fine columnar and equiaxial crystals due to the faster cooling rate, which enabled the oxidation and corrosion resistance to be improved. In the middle region, the cooling rate slowed down, and the coarse columnar crystals or dendrites were observed in some parts. Finally, there was a columnar/dendritic crystal growth in the bottom region, owing to the greater heat input close to the matrix.

(3) The self-corrosion potential of 2Cr13 stainless steel as the base material was −0.735 V, whereas those of Inconel 625 coatings prepared via laser cladding positively shifted throughout a range from −0.403 to −0.501 V. The corrosion current density of the substrate was found to be 6.32×10^{-6} A·cm^{-2}, and those of coatings ranged from 3.51×10^{-7} to 1.24×10^{-7} A·cm^{-2}, with a reduction of 94%–98%, greatly improving the corrosion resistance of the material. Thus, the optimized Inconel 625 coatings can significantly improve the corrosion resistance of 2Cr13 substrates, which is critical for extending blade life, especially in corrosive environments.

(4) The impact resistance data showed that specimens underwent the ductile fracture and performed well under impact loading without significant spalling and cracking. For instance, laser cladding of Inconel 625 significantly improved the impact resistance of the base 2Cr13 material (from 23% to 30%). This means that the repaired blades are able to withstand severe mechanical damage.

Author Contributions: Conceptualization, J.-T.Y., G.-D.Z. and Y.-H.Q.; data curation, Z.-L.C. and L.-S.W.; formal analysis, G.-D.Z.; investigation, Z.-L.C., Y.-H.Q. and H.D.; methodology, J.-T.Y., G.-D.Z. and Z.-L.C.; resources, J.-T.Y. and Y.-H.Q.; software, G.-D.Z., Z.-L.C. and Y.-H.Q.; validation, G.-D.Z. and L.-S.W.; writing—original draft, G.-D.Z.; writing—review and editing, J.-T.Y. and G.-D.Z. All authors have read and agreed to the published version of the manuscript.

Funding: This research received no external funding.

Institutional Review Board Statement: Not applicable.

Informed Consent Statement: Not applicable.

Data Availability Statement: Data will be made available on request.

Conflicts of Interest: The authors declare no conflict of interest.

References

1. Yang, J.Q.; Liu, Y.; Ye, Z.Y.; Yang, D.Z.; He, S.Y. Microstructure and tribological characteristics of nitrided layer on 2Cr13 steel in air and vacuum. *Surf. Coat. Technol.* **2009**, *204*, 705–712. [CrossRef]
2. Wen, Z.H.; Bai, J.F.; Yang, J. Effect of vacuum re-melting on the solid particles erosion behavior of Ni60-NiCrMoY composite coatings prepared by plasma spraying. *Vacuum* **2016**, *134*, 73–82. [CrossRef]
3. Turnball, A.; Zhou, S. Electrochemical short crack effect in environmentally assisted cracking of a steam turbine blade steel. *Corros. Sci.* **2012**, *58*, 33–40. [CrossRef]
4. Liu, M.X.; Ma, F.; Chang, G.R.; Fu, F.X.; Sastry Cheruvu, N.; Yu, L.J.; Dai, J.; Xu, K.W. Experimental investigation of failure behavior of the cracked 17-4PH steel blades in a top gas energy recovery turbine. *Eng. Fail. Anal.* **2019**, *105*, 545–554. [CrossRef]
5. Yang, K.; Jiang, Z.T.; Chen, C.; Zhang, S.H.; Liu, X. Investigation on the microstructure, tribological performance and corrosion resistance of Ni–Mo coatings deposited by HVOF and APS methods. *Vacuum* **2022**, *200*, 111023. [CrossRef]
6. Swadzba, L.; Formanek, B.; Gabriel, H.M.; Liberski, P.; Podolski, P. Erosion- and corrosion-resistant coatings for aircraft compressor blades. *Surf. Coat. Technol.* **1993**, *62*, 486–492. [CrossRef]
7. Ji, X.L.; Luo, C.Y.; Sun, Y.; Zhao, J.H. Corrosive wear of multi-layer Fe-based coatings laser cladded from amorphous powders. *Wear* **2019**, *438–439*, 203113. [CrossRef]
8. Chan, W.P.; Nana, K.A.; Min, G.L.; Jae, H.K.; Jeoung, H.K. Interfacial structure and pore formation mechanism during laser cladding of pure vanadium on Ti-6Al-4V alloy. *Int. J. Refract. Met. Hard Mater.* **2021**, *101*, 105671. [CrossRef]
9. Sattar, S.; Alaiwi, Y.; Radhi, N.S.; Al-Khafaji, Z.; Al-Hashimi, O.; Alzahrani, H.; Yaseen, Z.M. Corrosion reduction in steam turbine blades using nano-composite coating. *J. King Saud Univ.-Sci.* **2023**, *35*, 102861. [CrossRef]
10. Gong, K.F.; Zheng, C.B.; Ju, D.C.; Ma, H.; Zhang, J.M. Corrosion of Ni-based alloy coatings prepared by laser cladding in high-temperature chloride environment. *Surf. Coat. Technol.* **2024**, *484*, 130823. [CrossRef]
11. Yu, D.L.; Cheng, J.; Chu, Y.C.; Lan, W.; Zhang, H.W.; Zhou, X.; Jiang, Y.Y.; Dai, Q.W. Optimization of defects and high temperature corrosion resistance of laser cladding FeCrAl coatings: Influence of process parameters. *Opt. Laser Technol.* **2025**, *181*, 111640. [CrossRef]
12. Wu, Y.F.; Wu, X.M.; Li, L.C.; Li, B.; Wang, Z.H. Modeling of process parameters and wear performance investigation of Inconel 625 nickel-based coatings via laser cladding. *Opt. Laser Technol.* **2025**, *181*, 111749. [CrossRef]
13. Gao, J.; Ma, Q.C.; Sun, Y.; Wang, K.N.; Song, Q.; Wang, C.M. Effect of Nb content on microstructure and corrosion resistance of Inconel 625 coating formed by laser cladding. *Surf. Coat. Technol.* **2023**, *458*, 129311. [CrossRef]
14. Wu, X.M.; Li, B.; Wang, W.; Qi, S.Y.; Wu, Y.F.; Wang, Z.H. Corrosion behavior and mechanism of Inconel 625 coatings in high-temperature acidic environments for waste incineration applications. *Surf. Coat. Technol.* **2024**, *493*, 131291. [CrossRef]
15. Lei, Y.; Taheri, M.; Lashkari, A.H.; Torkamany, P.; Heidarpour, I.; Torkamany, M.J. Corrosion resistance of NbCrFeNiCoMoX coating applied by laser cladding on GTD-111 superalloy: Application of gas turbine blade. *Mater. Today Commun.* **2024**, *38*, 108157. [CrossRef]
16. Lv, Y.F.; Xu, P.; Liang, R.; Wang, L.; Pang, C. Corrosion resistance of VC-reinforced Fe-based SMA coatings by laser cladding. *Surf. Coat. Technol.* **2024**, *478*, 130457. [CrossRef]

17. Chen, B.; Zhang, G.S.; Zhang, Z.J.; Wang, Z.Y.; Guo, C.F.; Song, X.J. Improved wear and corrosion resistance of laser-clad (Fe0.25Co0.25Ni0.25Cr0.125Mo0.125)86B14 coating through annealing treatment. *Surf. Coat. Technol.* **2023**, *473*, 129973. [CrossRef]
18. Shan, B.; Chen, J.L.; Chen, S.Y.; Ma, M.Z.; Ni, L.L.; Shang, F.M.; Zhou, L. Laser cladding of Fe-based corrosion and wear-resistant alloy: Genetic design, microstructure, and properties. *Surf. Coat. Technol.* **2022**, *433*, 128117. [CrossRef]
19. He, Z.Y.; Zhan, D.X.; Yan, X.L.; Liu, W.; Tong, Y.G.; Liu, H.B.; Wang, K.M. Effect of oscillating laser cladding on microstructure and properties of stainless steel cladding layers. *Mater. Today Commun.* **2024**, *41*, 110254. [CrossRef]
20. *GB/T 1220-2007*; Stainless Steel Bars. Standardization Administration of China: Bejing, China, 2007. Available online: https://openstd.samr.gov.cn/bzgk/gb/newGbInfo?hcno=7C88197FD1C028E60E96B808D5D83FAC (accessed on 13 January 2025).
21. *GB/T229-2020*; Metal Materials-Charpy Pendulum Impact Test Method. Standardization Administration of China: Bejing, China, 2020. Available online: https://ebook.chinabuilding.com.cn/zbooklib/bookpdf/probation?SiteID=1&bookID=134020 (accessed on 13 January 2025).
22. Feng, K.; Chen, Y.; Deng, P.S.; Li, Y.Y.; Zhao, H.X.; Lu, F.G.; Li, R.F.; Huang, J.; Li, Z.G. Improved high-temperature hardness and wear resistance of Inconel 625 coatings fabricated by laser cladding. *J. Mater. Process. Technol.* **2017**, *243*, 82–91. [CrossRef]
23. Zhou, C.Y.; Zhao, S.S.; Wang, Y.B.; Liu, F.L.; Gao, W.Y.; Lin, X.C. Mitigation of pores generation at overlapping zone during laser cladding. *J. Mater. Process. Technol.* **2015**, *216*, 369–374. [CrossRef]
24. Haldar, B.; Saha, P. Identifying defects and problems in laser cladding and suggestions of some remedies for the same. *Mater. Today Proc.* **2018**, *5*, 13090–13101. [CrossRef]
25. Renu, K.; Sumit, K.; Alok, K.D.; Ananad, M.M.; Kumari, K. Microstructural characterization and corrosion analysis of HA/TiO_2 and HA/ZrO_2 composite coating on Ti-alloy by laser cladding. *Appl. Surf. Sci. Adv.* **2024**, *24*, 100655. [CrossRef]
26. Wei, M.; Li, J.; Xie, K.; Xiao, Y.Y.; Wan, Q.; Yang, Z.T.; Huang, Y.J.; Mohamed, R. Effect of WC content on hardness and fracture toughness of WC-Ni60A wear-resistant coatings. *Surf. Coat. Technol.* **2024**, *491*, 131133. [CrossRef]
27. Guo, L.L.; Zheng, H.L.; Liu, S.H.; Li, Y.Q.; Xu, X.D.; Feng, C.Y. Formation Quality Optimization and Corrosion Performance of Inconel 625 Weld Overlay Using Hot Wire Pulsed TIG. *Rare Met. Mater. Eng.* **2016**, *45*, 2219–2226. [CrossRef]
28. Wang, Q.; Li, Y.Y.; Yang, H.B. Effect of Laser Power on Laser Cladding Structure and Hardness of 17-4PH Wire. *Surf. Technol.* **2021**, *50*, 191–197. [CrossRef]
29. Wang, K.Y.; Yin, X.Q.; Li, C.X.; Du, K.P. Study on the thermal behavior and microstructure of Fe-based deposited layers prepared by laser cladding on Al substrate. *Opt. Laser Technol.* **2024**, *179*, 111365. [CrossRef]